

A 42 nJ/Conversion On-Demand State-of-Charge Indicator for Miniature IoT Li-Ion Batteries

Junwon Jeong¹, *Student Member, IEEE*, Seokhyeon Jeong², *Student Member, IEEE*,

Dennis Sylvester, *Fellow, IEEE*, David Blaauw³, *Fellow, IEEE*,

and Chulwoo Kim¹, *Senior Member, IEEE*

Abstract—An energy-efficient state-of-charge (SOC) indication algorithm and integrated system for low-power wireless sensor nodes with the miniature Internet of Things (IoT) batteries are introduced in this paper. Based on the key findings that the miniature Li-ion batteries exhibit a fast response to the battery current transient, we propose an instantaneous linear extrapolation (ILE) algorithm and circuit system based on the ILE algorithm allowing accurate on-demand estimation of SOC. Due to the on-demand operation, an always-ON current integration is avoided, reducing power and energy consumption by several orders of magnitude. Furthermore, the proposed SOC indicator does not require a battery disconnection from the load, ensuring continuous operation of the applications. The system is implemented in a 180-nm CMOS technology. The power consumption is 42 nW, and maximum SOC indication error is 1.7%. The minimum applicable battery capacity is as low as 2 μ Ah.

Index Terms—Battery, fuel gauge, Internet of Things (IoT), Li-ion battery, low power, state of charge (SOC), SOC indicator, wireless sensor node.

I. INTRODUCTION

MOST battery management systems require state-of-charge (SOC) indication, which keeps the track of a present charge inside the battery. The SOC information is used to dynamically control the charging and discharging operations of the battery, and it can be provided to the user. An accurate SOC indication is essential for applications where the battery is utilized as a power source. The indication error can be defined as a difference between the real SOC of the battery and the indicated SOC obtained by an SOC indicator (real SOC – indicated SOC). A positive error on

the SOC indication can make the application suddenly degrade its performance or even stop its operation, whereas sufficient charge remains in the battery. This may lead to using only a part of the available battery capacity, leading to recharging the battery more often than necessary. Therefore, the positive SOC indication error causes a premature wear-out of the battery. On the contrary, if a negative error on the SOC indication occurs, the application might keep operating even when the battery is empty. This leads to battery damage and malfunction of the application.

Low-power design techniques have led to very low-power wireless sensor nodes for Internet of Things (IoT) applications (4.7- μ W power consumption [1]). Therefore, the battery capacity requirements for IoT devices have also been relaxed (two 8- μ Ah Li-ion batteries [1]). At the same time, applications of IoT wireless sensor nodes are becoming more varied, often requiring the miniaturization of IoT sensor node systems (6 mm \times 5 mm \times 4 mm [1]). Furthermore, small-volume batteries have been introduced (1.7 mm \times 2.25 mm \times 0.2 mm [2]). As a result, small-capacity, miniature IoT batteries are increasingly used by these sensor nodes to reduce the total system volume. Besides, energy harvesting is often used in such systems, and battery levels fluctuate throughout the operation owing to diverse power draws and environment-dependent charging conditions. To enable the intelligent power management and dynamic control of performance, to avoid battery damage, and to increase the battery life time, it is essential to be able to accurately monitor the battery SOC with low-power consumption in the wireless sensor node for IoT applications. However, SOC indication techniques with sub-microwatt power consumption have not been reported yet (180 μ W in the normal mode [3]).

Many conventional approaches for battery SOC monitoring have been introduced. Battery impedance can be measured at a specific bias and various frequencies to indicate SOC, which is called impedance spectroscopy [4]. Measuring battery impedance as a function of frequency is not practical for portable devices, because it is difficult to apply a signal with a frequency sweep to the battery. An overall battery voltage relaxation behavior is measured for SOC indication, which is referred to as chronopotentiometry [5]. However, the implementation of this method is still expensive because all the battery voltage behaviors under various conditions (load currents, temperatures, SOC levels, and charging/discharging cycles) are stored in the memory. Other SOC indicators

Manuscript received April 17, 2018; revised July 15, 2018 and September 12, 2018; accepted October 4, 2018. Date of publication November 14, 2018; date of current version January 25, 2019. This paper was approved by Associate Editor Piero Malcovati. This work was supported in part by the National Research Foundation of Korea, Ministry of Science, ICT and Future Planning, Korean Government, under Grant 2016R1E1A1A02922127 and in part by the National Science Foundation of USA. (Corresponding author: Chulwoo Kim.)

J. Jeong is with the Department of Electrical Engineering, Korea University, Seoul 02841, South Korea, and also with the Department of Electrical Engineering and Computer Science, University of Michigan, Ann Arbor, MI 48109 USA (e-mail: jjw@kilby.korea.ac.kr).

S. Jeong, D. Sylvester, and D. Blaauw are with the Department of Electrical Engineering and Computer Science, University of Michigan, Ann Arbor, MI 48109 USA.

C. Kim is with the Department of Electrical Engineering, Korea University, Seoul 02841, South Korea (e-mail: ckim@korea.ac.kr).

Color versions of one or more of the figures in this paper are available online at <http://ieeexplore.ieee.org>.

Digital Object Identifier 10.1109/JSSC.2018.2876472

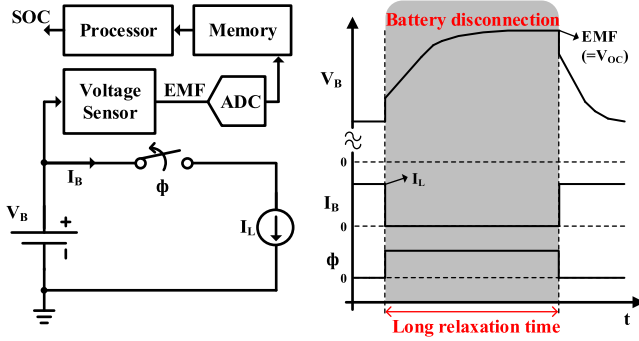


Fig. 1. Conventional SOC indicator: voltage relaxation method.

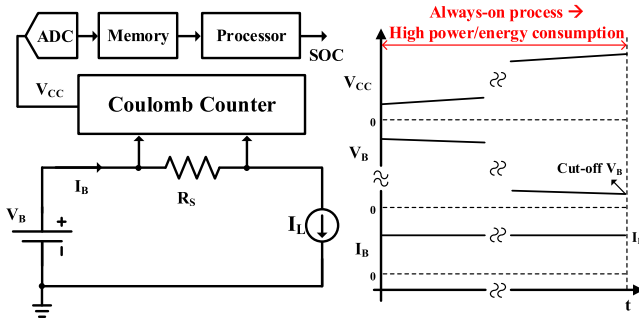


Fig. 2. Conventional SOC indicator: Coulomb counting.

have used algorithms based on fuzzy logic [6], [7], Kalman filters [8]–[11], or neural networks [12]–[15], which are too complex and expensive for implementation in integrated circuits. The electromotive force (EMF) of the battery, which is equivalent to the battery open-circuit voltage (V_{OC}), is widely known to accurately correlate with the battery SOC across age and temperature, for Li-ion and lead-acid batteries [5], [16], [17]. However, measuring the EMF, which is called voltage relaxation method (Fig. 1), requires a long relaxation time after the battery is disconnected from the load (typically 25 s for 12 μ Ah or 40 min for 4-Ah Li-ion batteries), which is problematic for continuously operating sensor nodes. Book-keeping algorithms based on the Coulomb counting (Fig. 2) are the most widely used approach to calculating SOC [3], [18]–[21], preventing the disconnection of the battery from the load. However, Coulomb counting is poorly suited to low-power sensor nodes, because battery current (I_B) monitoring (i.e., current integration) is an always-ON process that consumes significant power and energy (e.g., 180 μ W for all the battery run time [3]). Furthermore, these methods suffer from the charge error accumulation [5].

In this paper, we demonstrate an algorithm and a complete implementation for an accurate SOC indication with sub-microwatt power consumption. Our proposed instantaneous linear extrapolation (ILE) algorithm is based on directly estimating the EMF by modulating I_B . The proposed SOC indicator enables the on-demand operation, power-gating the system when an SOC indication is not needed. It allows system designers to reduce energy depending on how often the battery state information is required. Therefore, the battery usage

time can be significantly extended using the proposed SOC indicator. Furthermore, the proposed system does not require Coulomb counting, relaxation time, or disconnection of the battery from the load, ensuring continuous operation of the wireless sensor nodes.

Section II describes the concept of the on-demand direct EMF estimation with I_B modulation. Section III analyzes the I_B transient response of the battery and discusses the measured behaviors of large and small capacity batteries. Based on the analysis and the measurement results, key findings for small IoT batteries are derived. Section IV describes the proposed ILE algorithm based on the key findings and the direct EMF estimation with I_B modulation, enabling the accurate on-demand SOC indication. Section V highlights the issues pertaining to the circuit implementation of the ILE algorithm. Section VI presents the measurement results for a prototype chip. Finally, conclusions are listed in Section VII.

II. ON-DEMAND DIRECT EMF CALCULATION WITH I_B MODULATION

Fig. 3(a) shows the block diagram of the proposed SOC indicator, which consists of an I_B modulator, a voltage sensor, a current sensor, an analog-to-digital converter (ADC), a memory, and a processor [22]. A current draw of the wireless sensor node is modeled by a dc current source I_L . The system indicates SOC by directly calculating the EMF, which is strongly correlated with the battery SOC across the battery age and temperature [5], [16], [17]. Fig. 3(b) shows the operating waveforms of the proposed SOC indicator. Once a demand signal Φ is triggered during the normal operation of wireless sensor nodes, I_B modulator adjusts I_B by adding current I_{EX} for a short time duration of D_{IND} , which is negligible considering battery usage time. Battery voltage V_B and I_B behaviors during the I_B modulation are monitored to calculate the EMF of the battery. To sense the I_B behavior, the voltage difference across the current sensing resistor R_S ($V_B - V_{B_S}$) is changed to a proper range of input voltages for the subsequent ADC by the current sensor shown in Fig. 3. The unity gain buffers deliver the divided V_B and V_{B_S} to a switched capacitor amplifier in the current sensor. The switched capacitor amplifier in the current sensor modifies the divided V_B and V_{B_S} to proper voltage levels. At the same time, the voltage sensor modifies the level of V_B to conform to the following ADC input level. The switched capacitor amplifier in the voltage sensor changes the level of the divided V_B provided by the unity gain buffer. The single shared ADC digitizes both V_B and I_B by time multiplexing. The ADC outputs are stored in the memory. The processor directly calculates the EMF by the linear extrapolation of the two known points $[(I_L, V_L) \text{ and } (I_L + I_{EX}, V_{EX})]$ stored in the memory [Fig. 3(c)]. The system can repeat this single SOC indication with an indication frequency f_{IND} , which can be determined based on how often the battery SOC information is required.

The conventional SOC indications based on the Coulomb counting [3], [18]–[21] are an always-ON process, dissipating huge amounts of power and energy. Consequently, an effective battery usage time t_{USE} is small for miniature IoT batteries in

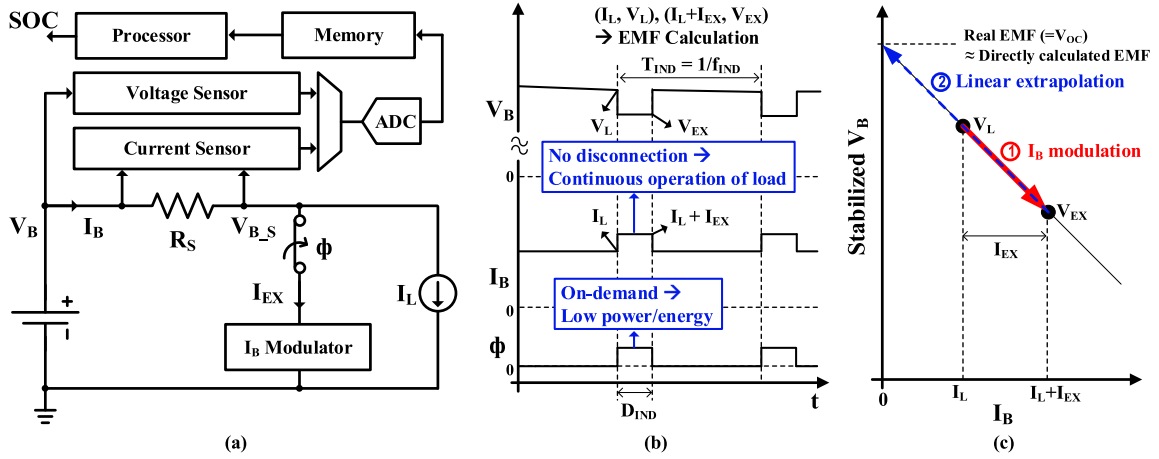


Fig. 3. Proposed SOC indicator. (a) Block diagram. (b) Operating waveforms. (c) Stabilized battery voltage (V_B) as a function of battery current (I_B).

low-power wireless sensor nodes that use this method. Time t_{USE} is defined as the number of available hours of battery uses while discharging the battery from 100% to 0% SOC. For simplicity, a V_B drop owing to the internal series resistance of the loaded battery is neglected in this derivation. Time t_{USE} with the Coulomb counting (t_{USE_CC}) is

$$t_{USE_CC} = \frac{Q_{tot}}{(I_L + I_Q)} \quad (1)$$

where Q_{tot} is the total charge in the battery at 100% SOC, I_Q is the current consumption of the SOC indicator, and I_L is the load current of the battery. For example, the Coulomb counting [3] consumes $50\text{-}\mu\text{A}$ I_Q . Assuming that a $12\text{-}\mu\text{Ah}$ Li-ion battery is applied with $10\text{-}\mu\text{A}$ I_L , the time t_{USE_CC} of [3] is only 12 min.

The proposed SOC indication enables the on-demand control, offering energy/power reduction by orders of magnitude. Energy/power consumptions can be reduced by adjusting f_{IND} . Time t_{USE} of the proposed on-demand SOC indication (t_{USE_PROP}) is

$$t_{USE_PROP} = \frac{Q_{tot}}{(I_L + I_Q \times D_{IND} \times f_{IND})} \quad (2)$$

where D_{IND} is determined at $200\text{ }\mu\text{s}$ for a $12\text{-}\mu\text{Ah}$ Li-ion battery by testing to minimize the indication error. Assuming that the SOC information is monitored once per second ($f_{IND} = 1\text{ Hz}$), $10\text{-}\mu\text{A}$ I_L is applied to a $12\text{-}\mu\text{Ah}$ Li-ion battery, and I_Q is $50\text{ }\mu\text{A}$, t_{USE_PROP} is 72 min, which is $12\times$ longer compared with the one of [3]. It should be noted that the on-demand control is not available with the conventional Coulomb counting because a Coulomb counter has to be connected to the battery and operate for all the battery run time.

Conduction losses across R_S with the proposed SOC indication and the conventional Coulomb counting are the same. Even though the target I_B range of the proposed system is much smaller, the proposed and the conventional works have the same relative power loss from R_S over the battery power, because the target battery power is also small. Therefore, avoiding the conduction loss from R_S can reduce the relative power loss. The conduction loss can be easily avoided by

simply implementing a bypass switch which is synchronized with demand signal for the indicator in parallel with R_S .

III. KEY FINDINGS FOR MINIATURE IOT BATTERIES

A. Battery I_B Transient Response

When I_B abruptly changes, the battery requires stabilization time τ for the stabilized V_B at the changed I_B [4]. As the capacity of the battery gets larger, the required τ increases due to the large surface area A of the electrode. After load is applied to the battery, the battery starts to convert the chemical energy to electrical one through charge-transfer reactions at $+$, $-$ electrode/electrolyte interfaces ($O + ne \leftrightarrow R$, O : oxidized species, R : reduced species, e : electrons, and n : the number of electrons involved in the charge-transfer reaction) [5]. Typical concentration profile of the oxidized species in the x -direction $c_O(x, t)$ in $[\text{mol}/\text{m}^3]$ when the I_B transient occurs is shown in Fig. 4 [4]. c_O^b is the electrolyte bulk concentration, and $c_O^s(t)$ represents the electrode surface concentration of oxidized species when $x = 0$. $\delta_O(t)$ is the diffusion layer thickness of the oxidized species in $[\text{m}]$. Based on the Sand equation [23], τ can be represented as

$$\tau = \left(\frac{nFA(c_O^b - c_O^s(\tau))\sqrt{D_0\pi}}{2I_L} \right)^2 \quad (3)$$

where F is Faraday's constant and D_0 is a diffusion coefficient in $[\text{m}^2/\text{s}]$, which is determined by the battery material. Assuming that the large- and small-capacity batteries have the same shape and the same chemical composition, D_0 , n , and c_O^b of both batteries can be considered to be equal. Large-capacity batteries show lower $c_O^s(\tau)$ compared with small-capacity batteries at given I_B [5]. Therefore, larger A of the large-capacity batteries yields longer τ compared with the small-capacity batteries if the same I_B transients are applied.

Fig. 5 shows the modeling of the loaded battery [5]. When the battery is disconnected from the load and is relaxed after sufficiently long relaxation time, the battery is in the state of equilibrium. Voltage V_B of the battery in the state of equilibrium is the same as its EMF ($= V_{OC}$). Potential drops

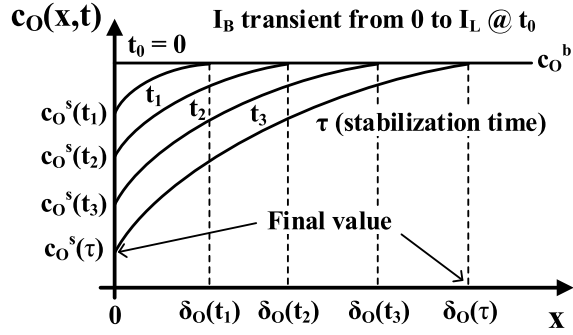
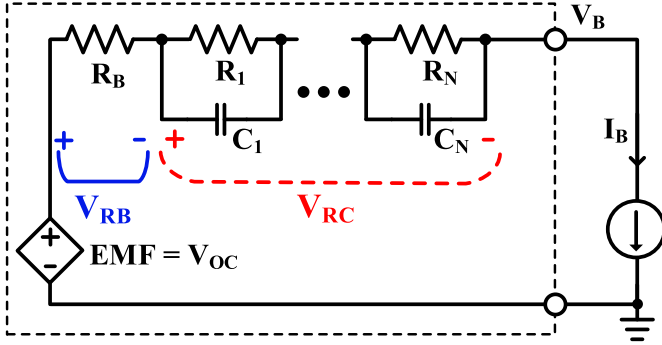
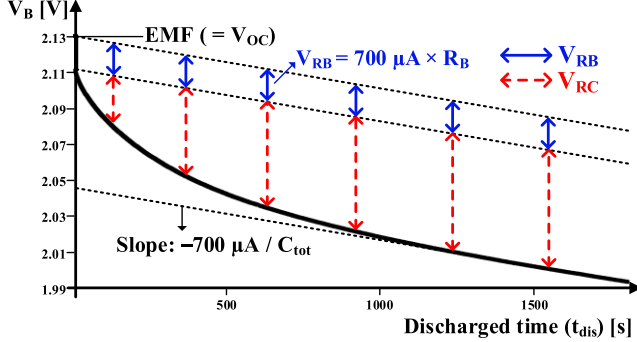
Fig. 4. Simplified concentration profile of oxidized species in the x -direction.

Fig. 5. Modeling of the loaded battery.

Fig. 6. Measured V_B across t_{dis} with large I_B transient (from 0 to 700 μA at 0 t_{dis}) using a 45-mAh Li-ion battery.

across resistive components (electrodes and electrolyte) can be modeled as a voltage drop V_{RB} across a single resistor R_B [5]. These potential drops are linear with respect to I_B and respond to the I_B transient immediately. The slow response to the I_B transient can be modeled as a voltage difference V_{RC} across several RC networks ($R_1, C_1, \dots, R_N, C_N$).

B. Battery Measurement Results

Fig. 6 shows the measured V_B versus the discharge time (t_{dis}) when I_B changes abruptly from 0 to 700 μA at 0 t_{dis} . A 45-mAh Li-ion battery [25] with the EMF of 2.13 V is tested at room temperature. Before discharging ($t_{dis} < 0$), the battery is in the state of equilibrium, and V_B at 0 t_{dis} is the same as the EMF. Immediately following the application of

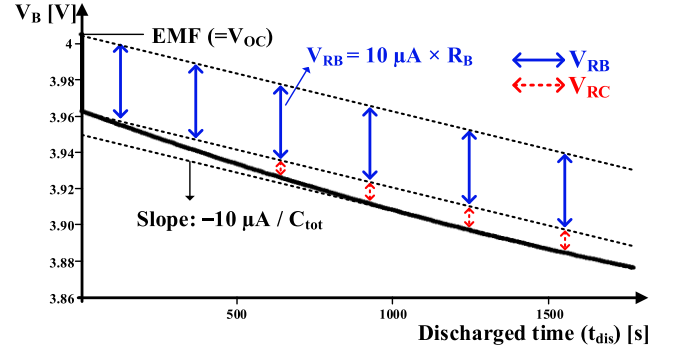
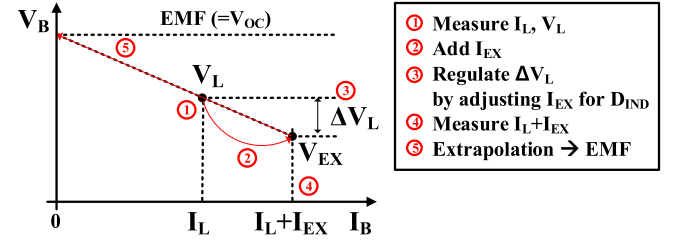
Fig. 7. Measured V_B across t_{dis} with small I_B transient (from 0 to 10 μA at 0 t_{dis}) using a 12- μA h Li-ion battery.

Fig. 8. Proposed ILE algorithm.

the I_B step, V_B decreases by $V_{RB}(= 700 \mu A \times R_B)$, which is time independent and constant across t_{dis} . As charge flows out from the battery at the rate of 700 $\mu C/s$ owing to the battery discharging, the slope of V_B will be $-700 \mu A / C_{tot}$, where C_{tot} is the effective total capacitance of the battery. However, the measured V_B slope is steeper than $-700 \mu A / C_{tot}$, owing to V_{RC} , which respond to I_L transient slowly. V_{RC} increases nonlinearly with t_{dis} because the battery requires τ for the stabilization. After the battery is stabilized, V_{RC} becomes constant. The V_B slope becomes equal to $-700 \mu A / C_{tot}$.

Fig. 7 shows the measured V_B versus t_{dis} , when the I_B step from 0 to 10 μA is applied at 0 t_{dis} . A miniature Li-ion battery (12 μA h, [26]) with the EMF of 4.01 V is measured at room temperature. As soon as I_B changes, V_B decreases immediately by $V_{RB}(= 10 \mu A \times R_B)$. V_{RB} remains constant during the battery discharging. In addition to this, V_B keeps decreasing due to the charge flowing out from the battery with the slope of $-10 \mu A / C_{tot}$. Contrary to the 45-mAh battery [25] with a 700- μA load step, V_B of the 12- μA h battery [26] has smaller V_{RC} and larger V_{RB} . Therefore, the 12- μA h Li-ion battery [26] is stabilized earlier than the 45-mAh battery.

Because the miniature IoT battery provides faster response to I_B transient, the on-demand direct EMF estimation with instant I_B modulation discussed in Section II can be effectively applied to small-capacity IoT batteries, as discussed in Section IV.

IV. PROPOSED ILE ALGORITHM

Fig. 8 shows the proposed ILE algorithm. In Section III, it was theoretically and experimentally verified that small IoT batteries quickly respond to I_B transients and exhibit

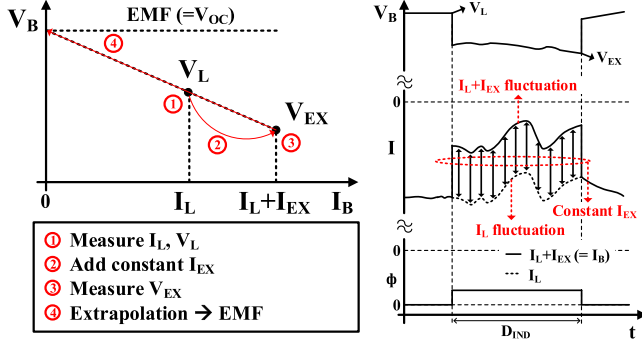


Fig. 9. Another possible algorithm: adding constant I_{EX} .

linear dependence between V_B and I_B . Based on these key findings and the on-demand direct EMF estimation using the I_B modulator in Section II, the ILE algorithm is proposed here. The ILE algorithm enables the indication system to operate on-demand, offering orders of magnitude reduction in the energy/power consumption without the Coulomb counter or disconnection of the battery. Once the on-demand signal is triggered, load current I_L is measured, and V_B at I_L , which is V_L , is also measured. Second, I_{EX} is added to I_L with the I_B modulator. The voltage difference between V_L and V_{EX} , which is ΔV_L , is regulated by adjusting I_{EX} with the I_B modulator. After the time duration D_{IND} , $I_L + I_{EX}$ is measured. Even though small IoT batteries exhibit small dependence on time, a minimal stabilization time D_{IND} is required for the batteries to be stabilized with the modulated I_B . The value of D_{IND} is determined to be 200 μs through battery testing, which emulates the I_B modulation with a source meter. The processor extrapolates from these two points, which are (I_L, V_L) and $(I_L + I_{EX}, V_{EX})$, to finally estimate the EMF.

I_L will naturally fluctuate as the sensor node performs various tasks. Fig. 9 shows the another possible algorithm for the on-demand direct EMF calculation with the I_B modulation. This algorithm adds constant I_{EX} , unlike the ILE algorithm. Therefore, if the I_L fluctuation occurs while the SOC indication is in progress, $I_L + I_{EX}$ also keeps changing. Owing to the I_B fluctuation, the battery cannot be stabilized with a single-modulated I_B . Therefore, the SOC indication will be inaccurate with this algorithm. However, the ILE algorithm regulates ΔV_L by adaptively controlling I_{EX} . Therefore, when I_L fluctuates, stable $I_L + I_{EX}$ can be guaranteed for the time duration D_{IND} using the ILE algorithm. Therefore, an accurate SOC indication is provided using the proposed ILE algorithm.

V. CIRCUIT IMPLEMENTATION

A. Top Architecture

Fig. 10 shows the top-level architecture of the complete SOC indicator based on the proposed ILE algorithm. Fig. 11 shows the timing diagram of the proposed SOC indicator. A 3-k Ω current-sensing resistor R_S senses I_B . C_L emulates the decoupling capacitance of the sensor node system while its current draw I_L is modeled by a dc current source. The whole system is turned off unless the power-gating signal

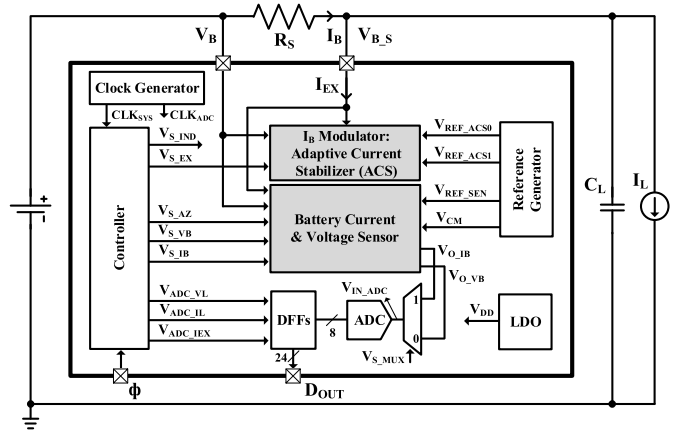


Fig. 10. Top architecture of the proposed SOC indicator.

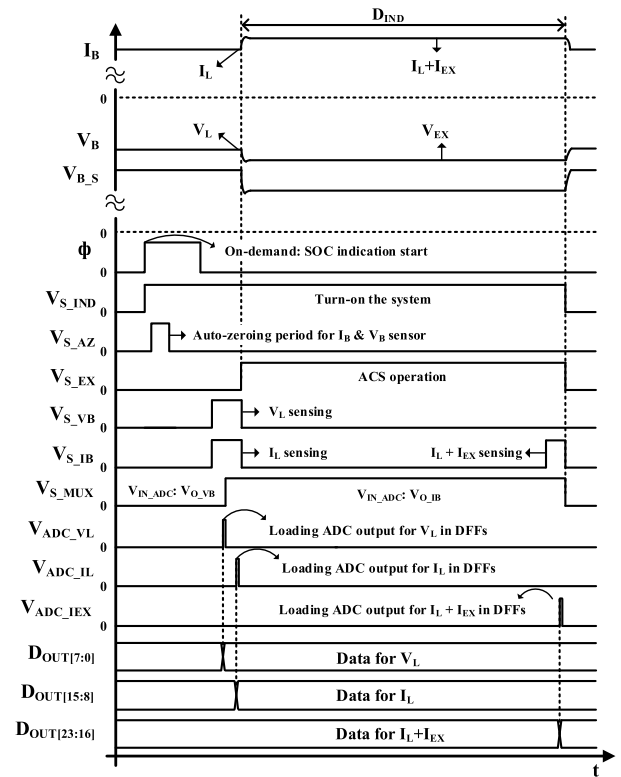


Fig. 11. Timing diagram of the proposed SOC indicator.

V_{S_IND} is set. At the rising edge of the on-demand signal Φ , which is applied from the outside of the indication system, the edge detector in the controller forces the LDO to generate the internal supply V_{DD} and V_{S_IND} is set to begin a single indication. The clock generator starts to provide a 100-kHz system clock (CLK_SYS) to the controller and an 800-kHz clock (CLK_ADC) to the ADC. After 1.5 cycles of CLK_SYS for system stabilization, V_{S_AZ} is set for the battery current and voltage (I_B and V_B) sensor to perform auto-zeroing. After auto-zeroing, V_{S_VB} and V_{S_IB} become “high” at the same time, and the I_B and V_B sensors sense V_L and I_L . V_L and I_L information are changed to proper input levels of the subsequent single-shared 8-bit ADC. The outputs of the I_B and

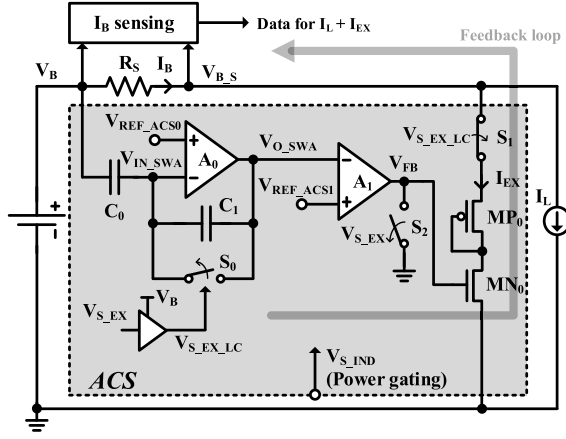


Fig. 12. Schematic of the ACS.

V_B sensor are denoted by V_{O_IB} and V_{O_VB} , respectively. The ADC digitizes V_{O_VB} first, and then the ADC output for V_L is loaded in D flip-flops (DFFs) at the rising edge of V_{ADC_VL} . V_{O_IL} with I_L information is also digitized through the ADC subsequently, and the output of ADC is stored in DFFs at the rising edge of V_{ADC_IL} . After these V_L and I_L sensing procedures are completed, the I_B modulator, which is called an adaptive current stabilizer (ACS), starts to operate and I_{EX} is additionally applied to the battery. The ACS adjusts the value of I_{EX} by regulating the difference between V_L and V_{EX} to be a reference voltage V_{REF_ACS1} . After 200- μs D_{IND} , V_{S_IB} is set again and $I_L + I_{EX}$ is sensed using the I_B sensor. The information about $I_L + I_{EX}$ is digitized using the ADC, and then the output of the ADC is stored in DFFs at the rising edge of V_{ADC_IEX} . The overall time for a single SOC indication operation is 350 μs . The ADC consumes 0.2 μA . Following this SOC indication operation, V_{S_IND} and V_{S_EX} become “low.” Therefore, the system is turned off and waits for the next rising edge of Φ . Owing to the timing issue associated with digital logic gates, one of the output values (8 bits of D_{OUT}) was not correctly latched by the on-chip DFFs and required external recording.

B. ACS

Fig. 12 shows the schematic of the ACS. One design challenge is that I_L will naturally fluctuate as the sensor node performs various tasks during the time duration D_{IND} . Accurate measurement of V_{EX} would, then, require an added stabilization time with a constant $I_L + I_{EX}$, which is impractical. We apply an adaptive I_{EX} to the battery by regulating the difference between V_L and V_{EX} to be the reference value, using the ACS. The ACS is composed of a switched capacitor amplifier, an error amplifier, and I_{EX} branch. The ACS is turned off unless V_{S_IND} is set. Fig. 13 shows the operating waveforms of the ACS. When V_{S_EX} is “low” and V_{S_IND} is “high,” a two-stage amplifier A_0 operates as a unity-gain amplifier. Therefore, the negative input of A_0 , which is V_{IN_SWA} , is regulated at V_{REF_ACS0} , and the voltage difference between V_B and V_{REF_ACS0} is stored in C_0 . V_{S_EX} is set, and then I_{EX} is additionally applied to the battery through I_{EX}

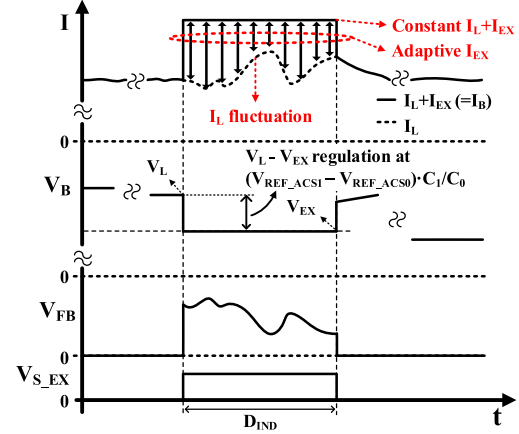


Fig. 13. Operating waveforms of the ACS.

branch composed of S_1 , MN_0 , and MP_0 , and V_B decreases. At the same time, switch S_0 is opened, and the switched capacitor amplifier (which consists of A_0 , C_0 , C_1 , and S_0) starts to operate. The difference between V_L and decreased V_B due to I_{EX} is amplified at the output of the switched capacitor amplifier V_{O_SWA} with the gain of C_0/C_1 and the voltage baseline of V_{REF_ACS0} . The value of V_{REF_ACS0} is determined at 2 V to maximize the accuracy of the switched capacitor amplifier. A level-shifted V_{S_EX} ($V_{S_EX_LC}$) is applied to S_0 and S_1 to fully turn off S_0 and S_1 . V_{O_SWA} is compared with the reference voltage V_{REF_ACS1} using a two-stage error amplifier A_1 . The output of A_1 (V_{FB}) is connected to the gate of MN_0 in the additional current I_{EX} branch. The feedback loop, which is composed of the switched capacitor amplifier, A_1 , and the I_{EX} branch, is built up. Therefore, the difference between V_L and decreased V_B due to I_{EX} (V_{EX}) is regulated at $(V_{REF_ACS1} - V_{REF_ACS0}) \cdot C_1/C_0$ by adjusting I_{EX} .

The values of V_{REF_ACS1} and C_0/C_1 should be determined carefully because these are highly related to the power dissipation and SOC indication accuracy. Larger V_{REF_ACS1} with fixed C_0/C_1 leads to larger $V_L - V_{EX}$. Because the dynamic range of I_B is much larger than the one of V_B , larger $V_L - V_{EX}$ requires much higher I_{EX} which increases the power consumption for the SOC indication. Similarly, smaller C_0/C_1 with fixed V_{REF_ACS1} yields larger $V_L - V_{EX}$, which also results in increased power consumption. Fig. 14 shows the average power consumption due to adding I_{EX} as a function of V_{REF_ACS1} and C_0/C_1 with 12- μAh [26] battery if f_{IND} and D_{IND} are 1 Hz and 200 μs , respectively. V_B is assumed to decrease linearly through 100% to 0% SOC for a simplicity. Therefore, an average V_B of 3.55 V is considered in this power consumption calculation. $I_{EX}/(V_L - V_{EX})$ is supposed to be 0.15 $\mu A/mV$ considering the measurement results of the 12- μAh battery [26]. The power consumed owing to I_{EX} branch is calculated to figure out the relationship between the power consumption, V_{REF_ACS1} and C_0/C_1 . On the other hand, small V_{REF_ACS1} or large C_0/C_1 yields small $V_L - V_{EX}$. This means that I_{EX} also becomes small, requiring a high-resolution ADC to digitize I_L and $I_L + I_{EX}$. The SOC indication accuracy

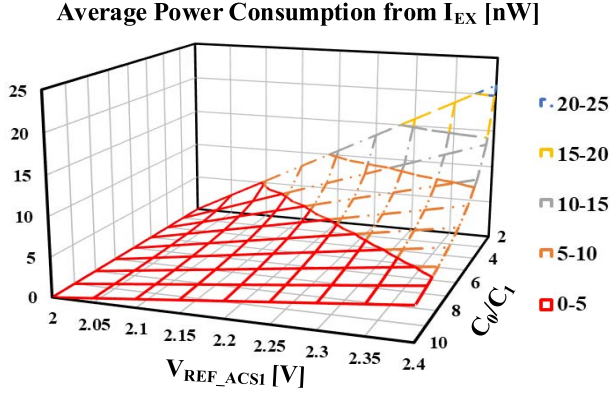


Fig. 14. Average power consumption from I_{EX} as a function of V_{REF_ACS1} and C_0/C_1 .

is dependent on the quantization error at ADC. The estimated EMF is

$$\text{Est. EMF} = \frac{(V_{REF_ACS1} - V_{REF_ACS0})C_1/C_0}{(I_L + I_{EX}) - I_L} I_L + V_L. \quad (4)$$

Considering the quantization error Q at digitizing current information, the estimated EMF can be represented as

$$\text{Est. EMF} = \frac{(V_{REF_ACS1} - V_{REF_ACS0})C_1/C_0}{(I_L + I_{EX} + I(Q_{IL+I_{EX}})) - (I_L + I(Q_{IL}))} \times (I_L + Q_{IL}) + V_L \quad (5)$$

where $Q_{IL+I_{EX}}$ and Q_{IL} are the quantization errors at $I_L + I_{EX}$ sensing and I_L sensing, respectively. The maximum quantization error in this paper is 1.15 mV because the ADC resolution is 2.3 mV. In the worst case, $Q_{IL+I_{EX}}$ and Q_{IL} are 1.15 and -1.15 mV, respectively. The SOC indication error (real EMF – estimated EMF) across V_{REF_ACS1} and C_0/C_1 in this worst case is shown in Fig. 15. V_L and $I_{EX}/(V_L - V_{EX})$ are considered to be 3.5 V and $0.15 \mu\text{A/mV}$, respectively. I_L is assumed to be $10 \mu\text{A}$. Furthermore, if V_{REF_ACS1} is small or C_0/C_1 is large, $V_L - V_{EX}$ should be regulated at a few millivolts, which is highly sensitive to the feedback errors (noise of node V_B or offsets of the feedback loop). These increase the design cost of the feedback loop. Fig. 16 shows the SOC indication error across V_{REF_ACS1} and C_0/C_1 with feedback errors. A voltage error of $500 \mu\text{V}$ at V_B node during the feedback loop operation is assumed. I_L and V_L are $10 \mu\text{A}$ and 3.5 V, respectively. V_{REF_ACS1} of 2.2 V and C_0/C_1 of 5 are used to provide 40-mV regulated $V_L - V_{EX}$ through the feedback loop. This yields 4.26-nW average power consumption due to I_{EX} , and the indication error less than 4 mV regarding the ADC quantization and the feedback errors. For example, a 50% SOC battery [26] at room temperature with $10\text{-}\mu\text{A}$ I_L yields $6\text{-}\mu\text{A}$ I_{EX} .

The loop stability of the ACS is dependent on four stages, which are the switched capacitor amplifier, the error amplifier, the I_{EX} branch, and the battery. When I_B abruptly changes, the battery overpotentials require an enough time to complete its response to the I_B transient. When V_B is 3.6 V, the simulated dc gain, the phase margin, and the gain margin of the feedback loop are 58 dB, 67° , and 21 dB, respectively. In this

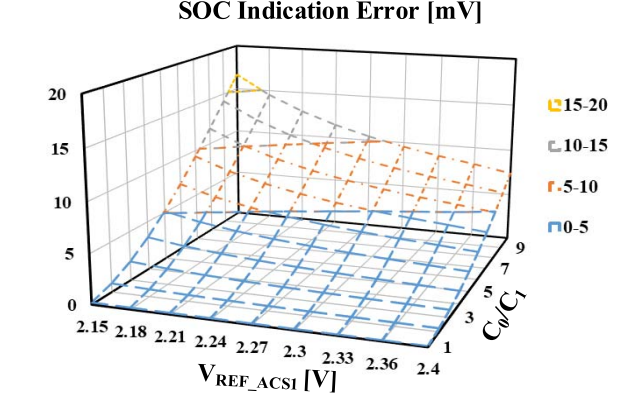


Fig. 15. SOC indication error as a function of V_{REF_ACS1} and C_0/C_1 with the quantization error at ADC.

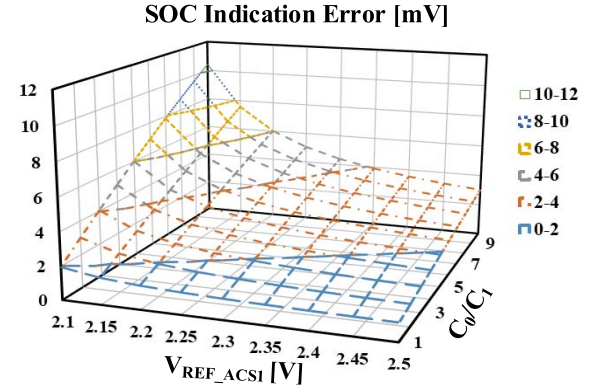


Fig. 16. SOC indication error as a function of V_{REF_ACS1} and C_0/C_1 with the feedback error.

simulation, the battery is modeled based on Fig. 5 where the voltage-source EMF is replaced with the voltage-controlled voltage source which is dependent on the SOC level with self-discharge.

Fig. 17 shows the simulated waveforms of the ACS when I_L abruptly changes during the SOC indication process. Rising/falling times of 100-ps and 10-pF C_L are assumed in this simulation. When a light-to-heavy I_L transition occurs at t_0 , the ACS reduces I_{EX} to maintain the desired $V_L - V_{EX}$ by decreasing V_{FB} . In a heavy-to-light I_L transient, I_{EX} is increased by the ACS to regulate $V_L - V_{EX}$ at the desired value. The maximum I_L transient amplitude that the ACS can manage is limited by: 1) The desired $V_L - V_{EX}$ value and 2) The current capability of I_{EX} branch shown in Fig. 12. First, the desired $V_L - V_{EX}$ value determines the maximum I_L transient amplitude when the light-to-heavy I_L transient occurs. In this paper, $V_L - V_{EX}$ is regulated at 40 mV, yielding $6\text{-}\mu\text{A}$ I_{EX} when $I_{EX}/(V_L - V_{EX})$ is supposed to be $0.15 \mu\text{A/mV}$. If the amplitude of the light-to-heavy I_L transient is larger than $6 \mu\text{A}$, the ACS cannot regulate $V_L - V_{EX}$, and $V_L - V_{EX}$ gets larger than 40 mV even though the feedback loop in the ACS turns off the I_{EX} branch. The maximum amplitude of the light-to-heavy I_L transient can be increased by applying

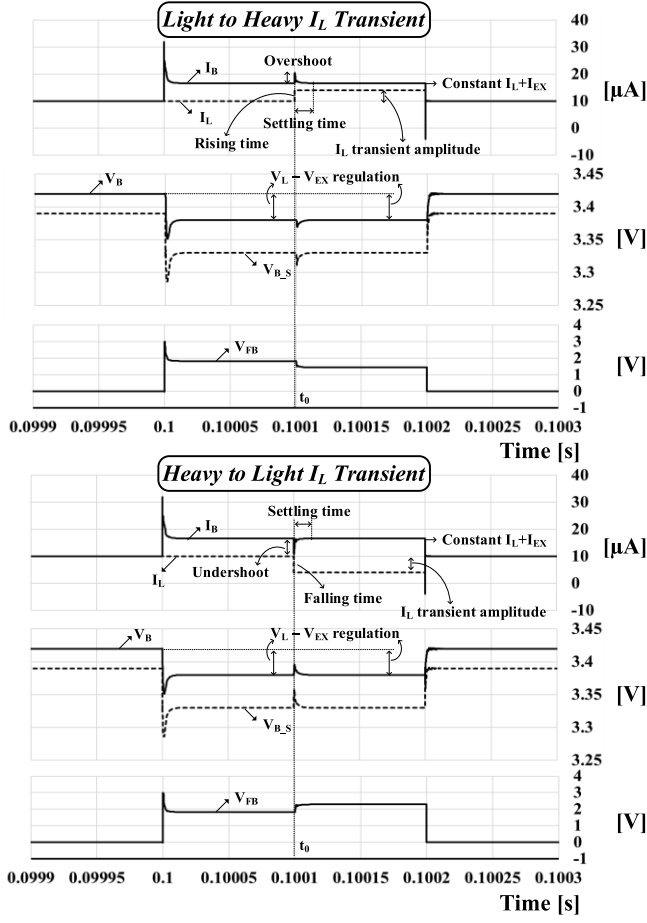


Fig. 17. Simulated waveforms of the ACS with I_L transient.

higher V_{REF_ACS1} at the expense of the power consumption, as shown in Fig. 14. Second, the current capability of I_{EX} branch limits the maximum amplitude of the heavy-to-light I_L transient. When the heavy-to-light I_L transition occurs during the ACS operation (Fig. 17), the ACS compensates the decreased I_L . If the amplitude of the heavy-to-light I_L transient is larger than the maximum current that the I_{EX} branch can provide, $I_L + I_{EX}$ cannot be the desired value for the $V_L - V_{EX}$ regulation even though the I_{EX} branch draws its maximum current. In this paper, the maximum amplitude of the heavy-to-light I_L transition that the ACS can compensate is $8 \mu A$. The maximum amplitude can be increased by increasing the MOSFET size of the I_{EX} branch.

Figs. 18 and 19 show the simulation results of the over/undershoots and settling time across the rising/falling times and C_L to discuss the speed of the ACS. Due to the limited speed of the feedback loop in the ACS, over/undershoot can occur and settling time can be required when I_L abruptly changes (Fig. 17). To verify the performance of the ACS in the worst case, the I_L transient amplitude is determined based on the discussion in the previous paragraph. The battery is modeled based on the testing results of the 12- μAh battery [26]. I_L before the transient is considered to be $10 \mu A$. In this simulation, settling time is defined as the required time after the I_L transient finishes, for regulated $I_L + I_{EX}$ to be settled within 1% of target $I_L + I_{EX}$. The settling time

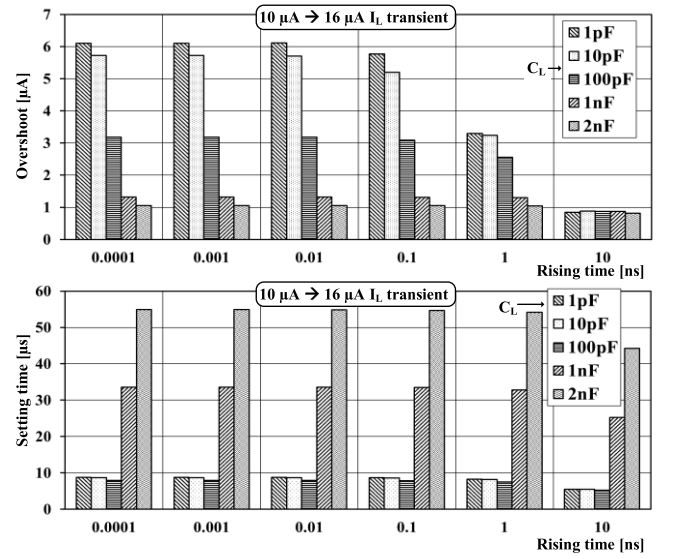


Fig. 18. Overshoot and settling time of the ACS across rising time and C_L when light-to-heavy I_L transient occurs.

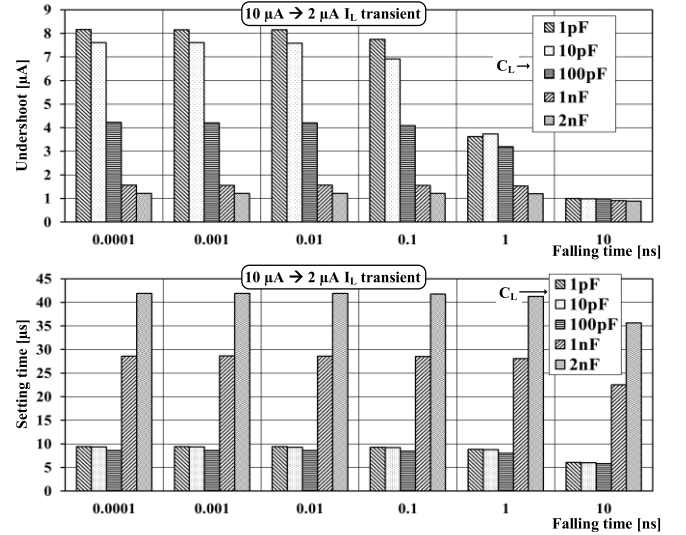
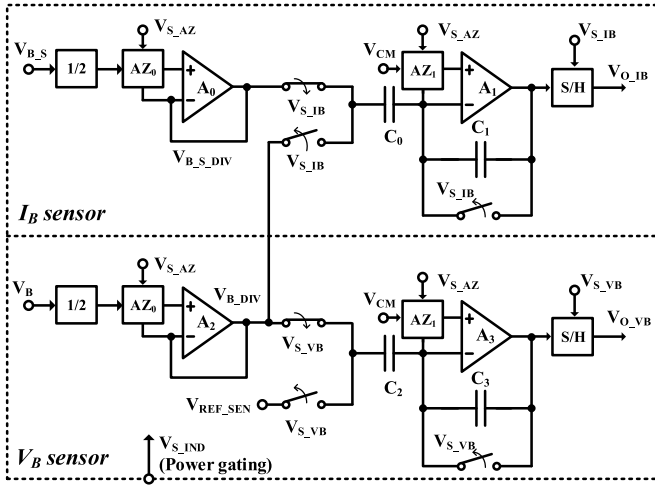


Fig. 19. Undershoot and settling time of the ACS across rising time and C_L when heavy-to-light I_L transient occurs.

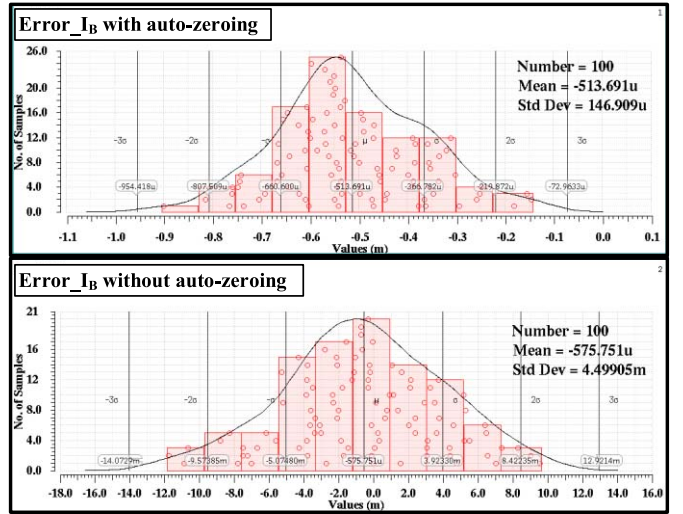
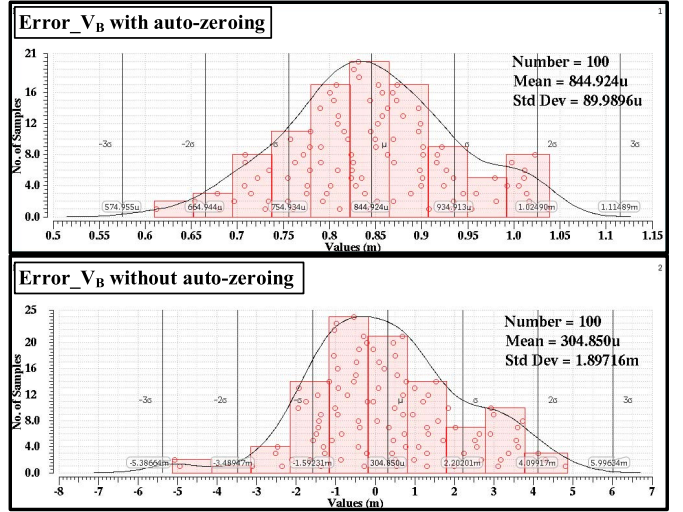
and over/undershoots mainly depend on the capacitance of C_L and the rising/falling times. As the rising/falling times increase, the over/undershoot decrease. The settling time also gets smaller as the rising/falling times increase. Furthermore, a larger C_L decreases the over/undershoots. However, the settling time gets worse as C_L gets larger. The large C_L slows down the battery response to I_{EX} change because the instant current change is supplied from C_L rather than the battery. The current consumptions of the switched capacitor amplifier and the error amplifier are 2 and $1.2 \mu A$ with 3-V supply, respectively.

C. I_B and V_B Sensors

Fig. 20 shows a schematic of the I_B and V_B sensors. The I_B and V_B sensors consist of dividers ($1/2$), unity-gain buffers with two-stage amplifiers (A_0 , A_2) and auto-zeroing

Fig. 20. Schematic of I_B and V_B sensor.

schemes (AZ_0), switched capacitor amplifiers with two-stage amplifiers (A_1 , A_3) and auto-zeroing schemes (AZ_1), and sample and hold circuits (S/H). The I_B and V_B sensors are turned off when V_{S_IND} is “low.” V_{S_IND} becomes set, and the I_B and V_B sensors start to operate. V_B and V_{B_S} are divided by half through diode-connected pMOS dividers to reduce the volume and power dissipation of the dividers. The unity-gain buffers provide the stable inputs for the switched capacitor amplifiers. The switched capacitor amplifiers adjust I_B and V_B information to the input range of the subsequent ADC. The S/H circuits store the outputs of the switched capacitor amplifiers. The outputs of the S/H circuits are connected to the ADC input. V_{S_AZ} becomes “high” to auto-zero the unity-gain buffers and switched capacitor amplifiers. When V_{S_IB} and V_{S_VB} are “low,” A_1 and A_3 operate as unity-gain buffers. Therefore, after the auto-zeroing period, the voltage difference between the output of A_2 (V_{B_DIV}) and the common-mode voltage (V_{CM}) is stored in C_0 . At the same time, the voltage difference between reference V_{REF_SEN} and V_{CM} is also stored in C_2 . Afterward, V_{S_IB} and V_{S_VB} are set simultaneously, and A_1 and A_3 start to function as a switched capacitor amplifier. Therefore, to generate data for I_B , the difference between V_{B_DIV} and $V_{B_S_DIV}$ is amplified by C_0/C_1 with the voltage baseline of V_{CM} . Following this amplification, the output of A_1 is sampled and provided to the ADC with the S/H circuit. At the same time, to generate data for V_B , the difference between V_{B_DIV} and V_{REF_SEN} is amplified with the gain of C_2/C_3 and the voltage baseline of V_{CM} . After the amplification period, the output of A_3 is connected to the S/H circuit and delivered to the ADC. The high accuracy is desired for current and voltage sensing to increase the SOC indication accuracy. Unfortunately, there is an input offset of the unit gain buffer and the switched capacitor amplifier, which is called V_{OFF} . These offsets degrade the SOC indication accuracy. The maximum SOC indication voltage error is -34.7 mV without auto-zeroing; this value is obtained based on simulations. Therefore, auto-zeroing schemes for the unity gain buffer and switched capacitor amplifier are implemented. AZ_0 and AZ_1 correspond to the auto-zeroing

Fig. 21. Monte Carlo simulation results of I_B sensor with auto-zeroing (top) and without auto-zeroing (bottom).Fig. 22. Monte Carlo simulation results of V_B sensor with auto-zeroing (top) and without auto-zeroing (bottom).

scheme for the unity gain buffer and the switched capacitor amplifier, respectively. Using these schemes, the maximum SOC indication voltage error is reduced to $264.5 \mu\text{V}$. Figs. 21 and 22 show the Monte Carlo simulation results of the I_B and V_B sensors with and without AZ_0 and AZ_1 . Errors in the I_B sensing (Error_{I_B}) and the V_B sensing (Error_{V_B}) are defined as ideal V_{O_IB} – simulated V_{O_IB} and ideal V_{O_VB} – simulated V_{O_VB} , respectively. Standard deviations (σ) of Error_{I_B} are $150 \mu\text{V}$ and 4.5 mV with and without the auto-zeroing schemes, respectively. Error_{V_B} shows σ of $90 \mu\text{V}$ and 1.9 mV with and without the auto-zeroing schemes, respectively. The current consumption of the I_B and V_B sensor is $16 \mu\text{A}$ with 3-V supply. Error on the resistance of R_S does not affect the indication error, because the I_B sensing errors due to the R_S error are canceled out based on (4).

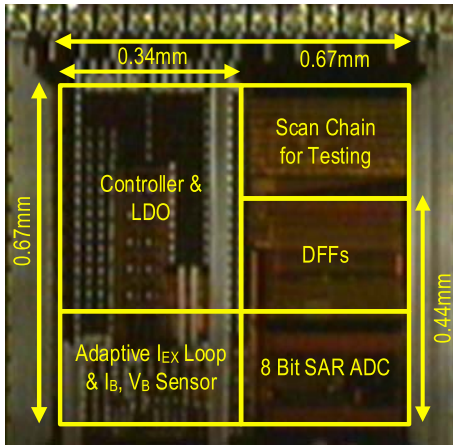


Fig. 23. Die photograph of the test chip.

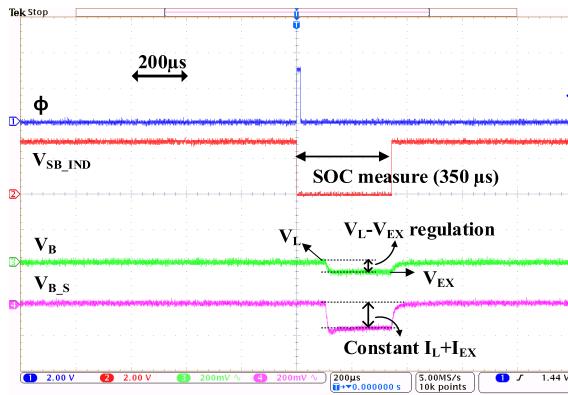
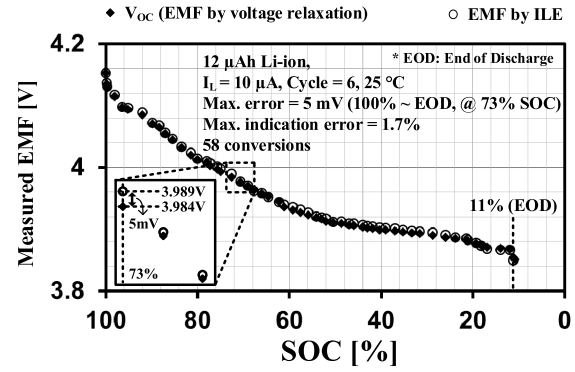
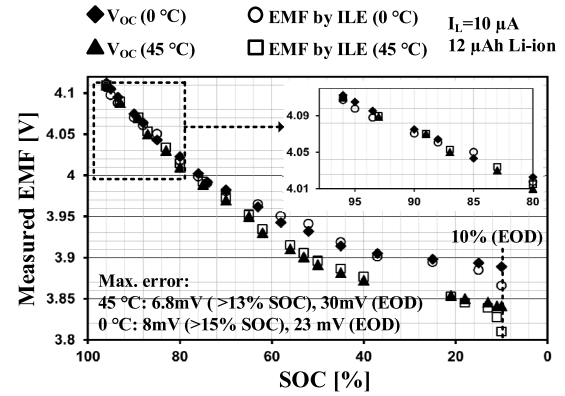


Fig. 24. Measured waveforms of the proposed SOC indicator.

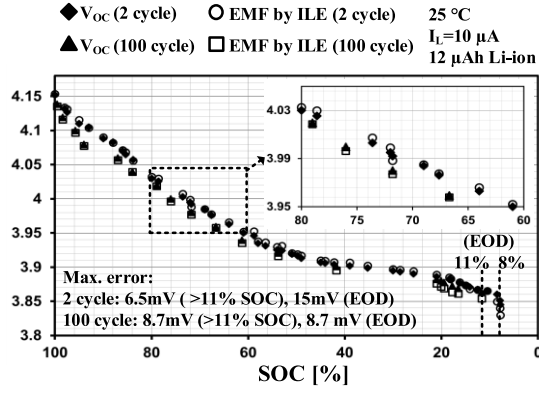
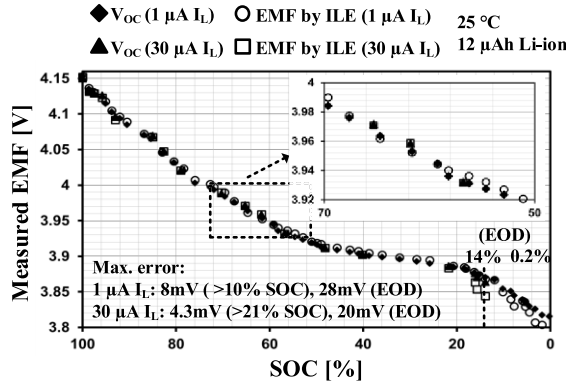
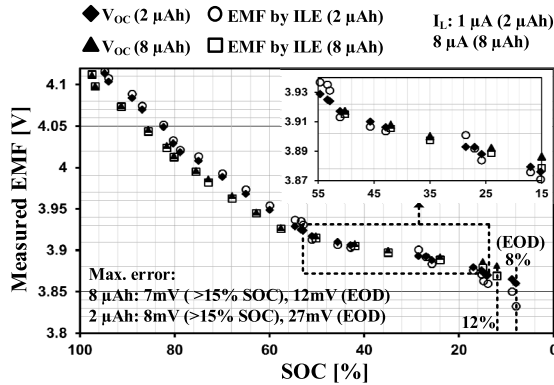
VI. MEASUREMENT RESULTS

The test chip micrograph is shown in Fig. 23. The proposed SOC indication system based on the ILE algorithm is implemented using a 180-nm CMOS technology. The system occupies 0.373 mm² active area. Fig. 24 shows the measured voltage waveforms. Once the on-demand signal Φ is triggered, SOC indication starts at the rising edge of Φ . The power-gating signal V_{SB_IND} goes low, and $V_L - V_{EX}$ is regulated by the ACS. Consequently, constant $I_L + I_{EX}$ is maintained. The 120 μ W is consumed for 350 μ s. Assuming a 1-Hz f_{IND} , this yields an average power consumption of 42 nW. System designers can select an appropriate tradeoff of average power with the rate of battery status updates.

Fig. 25 shows the measurement results of the implemented SOC indicator. To verify the system's accuracy, the EMF measured using the ILE is compared with V_{OC} obtained by the voltage relaxation method. At 10- μ A I_L , 6 cycles, and 25 $^{\circ}$ C temperature, the maximum indication error over V_{OC} is 5 mV, and the maximum indication error is 1.7%, which is defined as a difference between real SOC obtained from the V_{OC} curve and indicated SOC. The battery cannot be measured until 0% SOC because of the series resistance of the battery. At SOC region lower than 10%, the series resistance of the 12- μ Ah [26] battery is approximately 85 k Ω with 10- μ A I_L . The discharge cutoff voltage of the 12- μ Ah battery

Fig. 25. Measured EMF as a function of SOC, compared with V_{OC} .Fig. 26. Measured EMF across temperatures, compared with V_{OC} .

is 3 V. The 10- μ A I_L yields 0.85-V voltage drop. Therefore, EMF lower than 3.85 V cannot be measured due to the voltage drop across the series resistance. The lowest SOC limited by this series resistance is defined as the end of discharge (EOD). The value of the series resistance depends on SOC, I_L , temperature, cycle, etc. Fig. 26 shows the EMF measured using the ILE, as a function of SOC, for different temperatures. The maximum errors at 45 $^{\circ}$ C and 0 $^{\circ}$ C are 6.8 mV (>13% SOC) and 8 mV (>15% SOC), respectively. As SOC gets lower, the indication accuracy becomes worse due to the nonlinear overpotentials inside the battery which get larger as SOC decreases. This is because the bulk concentration of the reacting species and the exchange current become smaller at the lower SOC [5]. Furthermore, the time dependence of the electrode surface charge concentration gets worse at the lower SOC [4]. The maximum error at 0 $^{\circ}$ C is higher than the one at 45 $^{\circ}$ C because longer stabilization time is required for low temperature. Fig. 27 shows the EMF measured using the ILE, as a function of SOC, for different cycle counts. The maximum error is 8.7 mV (>11% SOC) for a 100 cycle battery. The EMF measured using the ILE, as a function of SOC, for various load currents, is shown in Fig. 28. With a 1- μ A load current, the maximum error is 8 mV (>10% SOC). The maximum error is 4.3 mV (>21% SOC) for a 30- μ A load current. Fig. 29 shows the EMF measured using the ILE, as a function of SOC with various types of batteries. The 2- [27] and 8- μ Ah [28] Li-ion batteries are measured. The maximum

Fig. 27. Measured EMF across cycles, compared with V_{OC} .Fig. 28. Measured EMF across I_L , compared with V_{OC} .Fig. 29. Measured EMF for different battery types, compared with V_{OC} .

errors for 8- and 2- μ Ah batteries are 7 and 8 mV at SOC larger than 11%, respectively.

To verify the feasibility of the proposed ILE algorithm with different batteries, the ILE algorithm is emulated with a source meter and automated testing. Fig. 30 shows the flowchart, timing diagram, and test setting of the emulated ILE algorithm. After the temperature chamber stabilization and battery charging, the battery is discharged continuously with I_L . Once the demand signal Φ sets, I_{EX} is additionally applied to the battery and EMF is calculated based on the ILE algorithm. Fig. 31 shows the measured indication error across V_{OC} and D_{IND} using the emulated ILE algorithm with

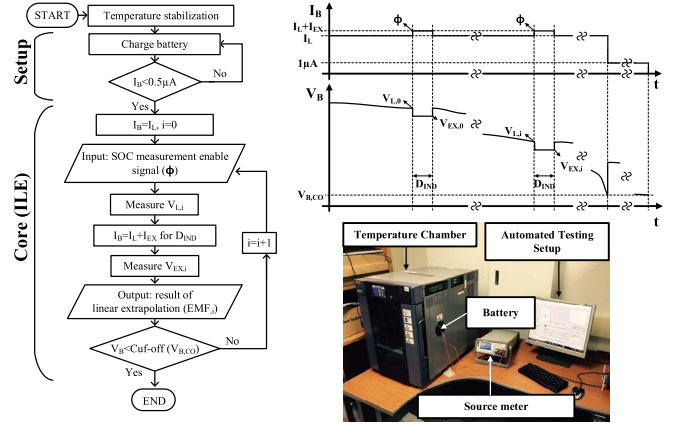
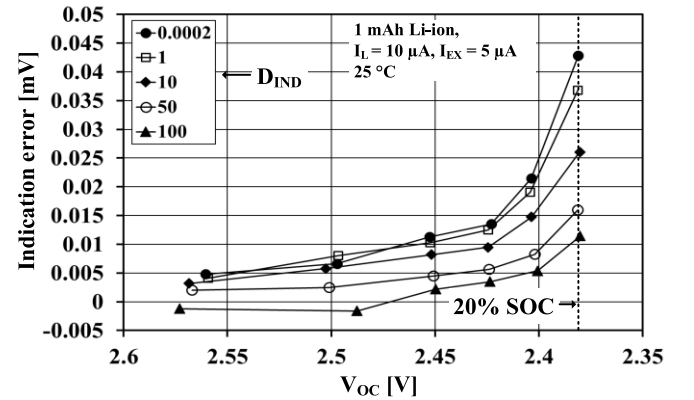


Fig. 30. Flowchart, timing diagram, and test setting to emulate the ILE algorithm.

Fig. 31. Measured indication error of the emulated ILE algorithm with a 1-mAh battery [29] and 5- μ A I_{EX} as a function of V_{OC} .

1-mAh lithium battery [29]. I_L and I_{EX} are 10 and 5 μ A, respectively. Larger D_{IND} enhances the indication accuracy because it helps the complete response of the battery to the I_B modulation. The EMF decrement owing to the larger D_{IND} is considerably small because the amount of equilibrium potential decrement due to I_{EX} is negligible ($<80 \mu$ V/s for the 1-mAh battery [29] with 10- μ A I_{EX}). As V_{OC} decreases, indication error gets larger because lower SOC yields higher nonlinear overpotentials [5]. Fig. 32 shows the measured indication error of the 1-mAh battery [29] across V_{OC} and D_{IND} using the emulated ILE algorithm when I_{EX} is large (90 μ A). The overall indication error increases because a longer time is required for the battery stabilization at 100- μ A $I_L + I_{EX}$. The target electrode surface concentration decreases at heavy I_B . Fig. 33 shows the measured EMF of emulated ILE algorithm with the 45-mAh [25] battery. I_L and I_{EX} are 700 and 200 μ A, because the 45-mAh battery has smaller V_B dynamic range at given I_B range compared with the 12- μ Ah battery. Therefore, 5- μ A I_{EX} causes V_B change less than 0.1 mV. Even though the small I_L and I_{EX} lead to high indication accuracy, this small amount of V_B change is hard to manage in the IC level. Owing to the large volume of the 45-mAh battery, the indication error gets worse. The proposed

TABLE I
COMPARISON TABLE

	bq26231 [18]	bq27426 [3]	bq2050 [21]	TCAS-1 [20]	ISSCC 2013 [19]	This work
Process	N/A	N/A	N/A	40-nm CMOS	130-nm CMOS	180-nm CMOS
Indication algorithm	Coulomb counting	Coulomb counting + voltage relaxation	Coulomb counting	Coulomb counting	Coulomb counting	ILE
Type	Continuous	Continuous	Continuous	Continuous	Continuous	<u>On-demand with no disconnection</u>
Power [μ W]	385 ⁽¹⁾	180 ⁽¹⁾	510 ⁽¹⁾	135	82.5	<u>0.042 @ $f_{IND}=1$ Hz</u>
Complete system	Yes	Yes ⁽²⁾	Yes	No ⁽³⁾	No ⁽³⁾	Yes
Indication error [%]	N/A ⁽⁴⁾	N/A ⁽⁴⁾	1.8 (0.2 C-rate, 25 °C)/ -16.7 (2.7 C-rate, 25 °C)/ 6.7 (0.2C-rate, -5 °C) ⁽⁵⁾	N/A ⁽⁴⁾	N/A ⁽⁴⁾	<u>1.7 (0.8 C-rate, 25 °C)/ -1 (2.5 C-rate, 25 °C)/ 6.1 (0.8 C-rate, 0 °C)⁽⁶⁾</u>
V_B [V]	2.8-5.5	2.45-4.5	3-6.5	2.5-3.3	N/A	3.2-4.2
R_S [Ω]	20 m	10 m	N/A	50 m	100 m	3 k

⁽¹⁾ Operating mode ⁽²⁾ Provides SOC and remaining capacity information

⁽³⁾ Only deals with coulomb counter ⁽⁴⁾ No indication error with real batteries is reported.

⁽⁵⁾ Error in empty estimation [17] with 720 mAh Li-ion batteries ⁽⁶⁾ Maximum error in real SOC (based on V_{OC}) – indicated SOC with 12 μ Ah Li-ion batteries

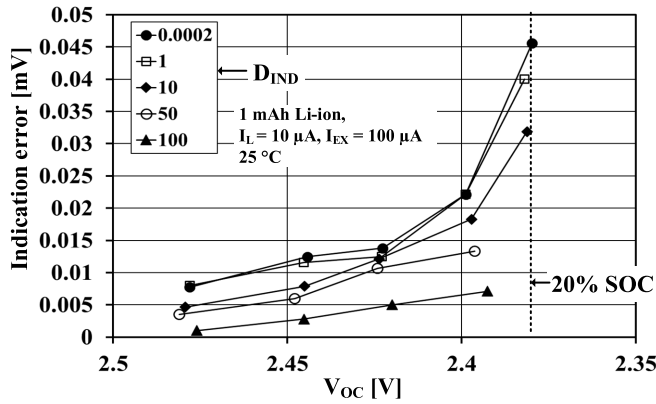


Fig. 32. Measured indication error of the emulated ILE algorithm with a 1-mAh battery [29] and 100- μ A I_{EX} as a function of V_{OC} .

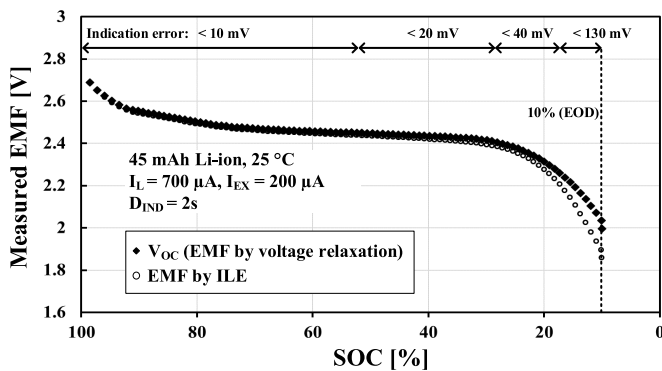


Fig. 33. Measured EMF with the emulated ILE algorithm with a 45-mAh battery [25] as a function of SOC.

ILE algorithm can be applied to the 45-mAh battery at the SOC region larger than 55% with the indication error of less than 10 mV.

Table I provides a performance comparison table including several conventional SOC indicators implemented in integrated

circuits. The proposed technique enables the on-demand operation and offers several orders of magnitude reduction in power, enabling the accurate SOC indication of miniature IoT batteries while other techniques are not applicable for these batteries owing to the high power consumption. Furthermore, no disconnection between the battery and the load is required. The -1% maximum SOC indication error is measured at 30- μ A I_L (2.5 C-rate of 12- μ Ah Li-ion batteries [26]) and 25 °C. Furthermore, 1.7% and 6.1% maximum SOC indication errors are measured at 25 °C and 0 °C, respectively, at 0.2 C-rate.

VII. CONCLUSION

An ultralow-power SOC indication algorithm and integrated system for the miniature IoT batteries are introduced in this paper. Based on the key findings of the miniature IoT batteries, on-demand direct EMF calculation with I_B modulation is proposed, which is called ILE algorithm. The on-demand SOC indication offers several orders of magnitude reduction in power/energy, which significantly extends usage time of the miniature IoT batteries. The ILE algorithm itself is experimentally verified. The ILE algorithm is implemented in integrated circuits using a 180-nm CMOS technology. The ACS regulates $V_L - V_{EX}$ rather than I_{EX} to modulate I_B , enhancing SOC indication accuracy under battery load current fluctuation. I_B and V_B information are accurately digitized using I_B and V_B sensors with auto-zeroing schemes. The implemented system consumes 42 nW assuming 1-Hz f_{IND} . The maximum SOC indication error is 1.7% with 12- μ Ah miniature battery. SOC indication accuracy using the proposed system across various conditions (SOC levels, temperatures, cycles, load currents, and battery capacities) is experimentally verified. Furthermore, the system does not require battery disconnection, relaxation time, and always-ON current integration. The minimum applicable battery capacity is as low as 2 μ Ah due to the low power/energy consumption and the high accuracy.

REFERENCES

- [1] M. Cho *et al.*, "A $6 \times 5 \times 4 \text{ mm}^3$ general purpose audio sensor node with a $4.7 \mu\text{W}$ audio processing IC," in *Proc. VLSI Circuits Symp.*, Jun. 2017, pp. C312–C313.
- [2] *Rechargeable Solid Stage Energy Storage: 5 μAh , 3.8 V, EnerChip CBC005 Datasheet*, Cymbet Corp., Elk River, MN, USA, 2012.
- [3] *System-Side Impedance TrackTM Fuel gauge bq27426 Datasheet*, Texas Instrum., Dallas, TX, USA, 2017.
- [4] A. J. Bard and L. R. Faulkner, *Electrochemical methods: Fundamentals and Applications*. New York, NY, USA: Wiley, 1980.
- [5] H. J. Bergveld, W. S. Kruijt, and P. H. L. Notten, *Battery Management Systems: Design by Modelling*. Dordrecht, The Netherlands: Kluwer, 2002.
- [6] A. J. Salkind, C. Fennie, P. Singh, T. Atwater, and D. E. Reisner, "Determination of state-of-charge and state-of-health of batteries by fuzzy logic methodology," *J. Power Sources*, vol. 80, nos. 1–2, pp. 293–300, 1999.
- [7] P. Singh, R. Vinjamuri, X. Wang, and D. Reisner, "Design and implementation of a fuzzy logic-based state-of-charge meter for Li-ion batteries used in portable defibrillators," *J. Power Sources*, vol. 162, no. 2, pp. 829–836, 2006.
- [8] G. L. Plett, "Extended Kalman filtering for battery management systems of LiPB-based HEV battery packs: Part 1. Background," *J. Power Sources*, vol. 134, no. 2, pp. 252–261, 2004.
- [9] G. L. Plett, "Extended Kalman filtering for battery management systems of LiPB-based HEV battery packs: Part 2. Modeling and identification," *J. Power Sources*, vol. 134, no. 2, pp. 262–276, 2004.
- [10] G. L. Plett, "Extended Kalman filtering for battery management systems of LiPB-based HEV battery packs: Part 3. State and parameter estimation," *J. Power Sources*, vol. 134, no. 2, pp. 277–292, 2004.
- [11] J. Garche and A. Jossen, "Battery management systems (BMS) for increasing battery life time," in *Proc. IEEE 3rd Int. Telecommun. Energy Special Conf. (TELESCON)*, May 2000, pp. 81–88.
- [12] O. Gerard, J. N. Patillon, and F. d'Alché-Buc, "Neural network adaptive modeling of battery discharge behavior," in *Proc. Int. Conf. Artif. Neural Netw.*, in Lecture Notes in Computer Science, vol. 1327, Jun. 2005, pp. 1000–1095.
- [13] W. X. Shen, C. C. Chan, E. W. C. Lo, and K. T. Chau, "A new battery available capacity indicator for electric vehicles using neural network," *Energy Convers. Manage.*, vol. 43, no. 6, pp. 817–826, 2002.
- [14] Y. Shen, "Adaptive online state-of-charge determination based on neuro-controller and neural network," *Energy Convers. Manage.*, vol. 51, no. 5, pp. 1093–1098, 2010.
- [15] C. Chan, E. W. C. Lo, and S. Weixiang, "The available capacity computation model based on artificial neural network for lead-acid batteries in electric vehicles," *J. Power Sources*, vol. 87, nos. 1–2, pp. 201–204, 2000.
- [16] J. H. Aylor, A. Thieme, and B. W. Johnso, "A battery state-of-charge indicator for electric wheelchairs," *IEEE Trans. Ind. Electron.*, vol. 39, no. 5, pp. 398–409, Oct. 1992.
- [17] F. A. C. M. Schoofs, W. S. Kruijt, R. E. F. Einerhand, S. A. C. Hanneman, and H. J. Bergveld, "Method of and device for determining the charge condition of a battery," U.S. Patent 6420851 B1, Apr. 4, 2000.
- [18] *Low-Cost Battery Coulomb Counter for Embedded Portable Applications bq26231 Datasheet*, Texas Instrum., Dallas, TX, USA, 2017.
- [19] S. H. Shalmany *et al.*, "A micropower battery current sensor with $\pm 0.03\%$ (3σ) inaccuracy from -40 to $+85^\circ\text{C}$," in *IEEE ISSCC Dig. Tech. Papers*, Feb. 2013, pp. 386–387.
- [20] F. Neri and L. Cimaz, "40 nm CMOS ultra-low power integrated gas gauge system for mobile phone applications," *IEEE Trans. Circuits Syst. I, Reg. Papers*, vol. 60, no. 4, pp. 836–845, Apr. 2013.
- [21] *Lithium Ion Power GaugeTM IC bq2050 Datasheet*, Texas Instrum., Dallas, TX, USA, 2017.
- [22] J. Jeong, S. Jeong, C. Kim, D. Sylvester, and D. Blaauw, "A 42nJ/conversion on-demand state-of-charge indicator for miniature IoT Li-ion batteries," in *Proc. Symp. VLSI Circuits*, Jun. 2017, pp. 206–207.
- [23] H. J. S. Sand, "III. On the concentration at the electrodes in a solution, with special reference to the liberation of hydrogen by electrolysis of a mixture of copper sulphate and sulphuric acid," *Phil. Mag.*, vol. 1, no. 1, pp. 45–79, 1901.
- [24] D. Linden, *Handbook of Batteries*, 2nd ed. New York, NY, USA: McGraw-Hill, 1995.
- [25] *Manganese Lithium Coin Batteries ML2020 Datasheet*, Panasonic, Osaka, Japan, 2005.
- [26] *Rechargeable Solid Stage Energy Storage: 12 μAh , 3.8 V, EnerChip CBC012 Datasheet*, Cymbet Corp., Elk River, MN, USA, 2009.
- [27] *Rechargeable Solid Stage Energy Storage: 2 μAh , 3.8 V, EnerChip CBC002 Datasheet*, Cymbet Corp., Elk River, MN, USA, 2012.
- [28] *Rechargeable Solid Stage Energy Storage: 8 μAh , 3.8 V, EnerChip CBC008 Datasheet*, Cymbet Corp., Elk River, MN, USA, 2012.
- [29] *High Capacity, Pb-Free Reflowable Rechargeable Battery ML414H Datasheet*, Seiko Instrum. Inc., Chiba, Japan, 2005.



Junwon Jeong (S'12) received the B.S. degree in electrical engineering from Korea University, Seoul, South Korea, in 2012, where he is currently pursuing the Integrated M.S. and Ph.D. degrees.

His research interests include integrated power management system designs, low-voltage low-power CMOS analog circuit designs, energy harvesting circuit designs, and fuel gauging circuit design.



Seokhyeon Jeong (S'12) received the B.S. degree in electrical engineering from the Korea Institute of Science and Technology, Seoul, South Korea, in 2011, and the Ph.D. degree in electrical engineering from the University of Michigan, Ann Arbor, MI, USA, in 2017.

He is currently with CubeWorks, Ann Arbor, where he is involved in researching and developing interface circuits for ultralow-power sensor nodes. His research interests include ultralow-power temperature sensor, A/D converter, and the design of millimeter-scale computing systems.



Dennis Sylvester (S'95–M'00–SM'04–F'11) received the Ph.D. degree in electrical engineering from the University of California at Berkeley, Berkeley, CA, USA.

He co-founded Ambiq Micro, a fabless semiconductor company developing ultralow-power mixed-signal solutions for compact wireless devices. He has held research staff positions at the Advanced Technology Group of Synopsys, Mountain View, CA, USA, and Hewlett-Packard Laboratories, Palo Alto, CA, USA, and visiting professorships at the National University of Singapore, Singapore, and Nanyang Technological University, Singapore. He is currently a Professor of electrical engineering and computer science with the University of Michigan, Ann Arbor, MI, USA, where he also the Director of the Michigan Integrated Circuits Laboratory, a group of 10 faculty and more than 70 graduate students. He has authored over 450 articles along with one book and several book chapters. He holds 37 U.S. patents. His research interests include the design of millimeter-scale computing systems and energy-efficient near-threshold computing. He also serves as a Consultant and Technical Advisory Board Member for electronic design automation and semiconductor firms in these areas.

Dr. Sylvester was a recipient of the NSF CAREER award, the Beatrice Winner Award at ISSCC, the IBM Faculty Award, the SRC Inventor Recognition Award, and 10 best paper awards and nominations. His dissertation was recognized with the David J. Sakrison Memorial Prize as the most outstanding research from the UC-Berkeley EECS Department. He was named as one of the top contributing authors at ISSCC, most prolific author at the IEEE Symposium on VLSI Circuits, and was awarded the University of Michigan Henry Russel Award for Distinguished Scholarship. He served on the Executive Committee for the ACM/IEEE Design Automation Conference. He serves on the Technical Program Committee for the IEEE International Solid-State Circuits Conference. He serves as an Associate Editor for the *IEEE Journal of Solid-State Circuits*, the *IEEE TRANSACTIONS ON CAD*, and the *IEEE TRANSACTIONS ON VLSI SYSTEMS*. From 2016 to 2017, he was a Distinguished Lecturer of the IEEE Solid-State Circuits Society.



David Blaauw (M'94–SM'07–F'12) received the B.S. degree in physics and computer science from Duke University, Durham, NC, USA, in 1986, and the Ph.D. degree in computer science from the University of Illinois at Urbana–Champaign, IL, USA, in 1991.

Until 2001, he was the Manager with the High Performance Design Technology Group, Motorola, Inc., Austin, TX, USA. Since 2001, he has been with the Faculty of the University of Michigan, Ann Arbor, MI, USA, where he is currently a Professor.

He has extensive research in ultralow-power computing using subthreshold computing and analog circuits for millimeter sensor systems and for high-end servers, his research group and collaborators introduced the so-called near-threshold computing, which has become a common concept in the semiconductor design. This work led to a complete sensor node design with record low-power consumption, which was selected by the MIT Technology Review as one of the year's most significant innovations. Most recently, he has pursued research in cognitive computing using analog, in-memory neural networks. He has authored over 500 papers, has received numerous best paper awards and nominations, and holds 60 patents. His research has a threefold focus.

Dr. Blaauw has investigated adaptive computing to reduce margins and improve energy efficiency using a new approach he pioneered, called Razor, for which he received the Richard Newton GSRC Industrial Impact Award and the IEEE Micro Annual Top-Picks Award. He received the 2016 SIA-SRC Faculty Award for lifetime research contributions to the U.S. Semiconductor Industry and the Motorola Innovation Award. He was the General Chair of the IEEE International Symposium on Low Power and the Technical Program Chair of the ACM/IEEE Design Automation Conference. He serves on the Technical Program Committee for the IEEE International Solid-State Circuits Conference.



Chulwoo Kim (S98–M02–SM06) received the B.S. and M.S. degrees in electronics engineering from Korea University, Seoul, South Korea, in 1994 and 1996, respectively, and the Ph.D. degree in electrical and computer engineering from the University of Illinois at Urbana–Champaign, IL, USA, in 2001.

In 1999, he joined Design Technology, Intel Corporation, Santa Clara, CA, USA, as an Intern. In 2001, he joined the IBM Microelectronics Division, Austin, TX, USA, where he was involved in cell processor design. He was a Visiting Professor

with the University of California at Los Angeles, Los Angeles, CA, USA, in 2008, and also with the University of California at Santa Cruz, Santa Cruz, CA, USA, in 2012. Since 2002, he has been with the School of Electrical Engineering, Korea University, where he is currently a Professor. He has co-authored two books, namely, *CMOS Digital Integrated Circuits: Analysis and Design* (McGraw Hill, 2014, fourth edition) and *High-Bandwidth Memory Interface* (Springer, 2013). His current research interests include wireline transceivers, memory, power management, and data converters.

Dr. Kim received the Samsung HumanTech Thesis Contest Bronze Award in 1996, the ISLPED Low-Power Design Contest Award in 2001 and 2014, the DAC Student Design Contest Award in 2002, the SRC Inventor Recognition Awards in 2002, the Young Scientist Award from the Ministry of Science and Technology, South Korea in 2003, the Seoktop Award for excellence in teaching in 2006 and 2011, the ASP-DAC Best Design Award in 2008, the Special Feature Award in 2014, and the Korea Semiconductor Design Contest: Ministry of Trade, Industry and Energy Award in 2013. From 2015 to 2016, he was a Distinguished Lecturer of the IEEE Solid-State Circuits Society. He served on the Technical Program Committee for the IEEE International Solid-State Circuits Conference. He served as a Guest Editor for the *IEEE Journal of Solid-State Circuits*. He is currently on the Editorial Board of the IEEE TRANSACTIONS ON VLSI SYSTEMS.